Comparative Performance Evaluation of Wound Rotor Synchronous Motor and Interior Permanent Magnet Synchronous Motor with Experimental Verification

Yu-Seop PARK
Department of Electrical Engineering, Korea National University of Transportation, Chungju, Korea
yspark @ut.ac.kr

***Abstract*—This paper deals with the comparison and performance evaluation of a wound rotor synchronous motor (WRSM) and an interior permanent magnet synchronous motor (IPMSM) based on electromagnetic field characteristic analysis. The models have identical stator structure with three-phase coil winding while the rotor outer diameter and stack length are under same condition. Based on surface response method, each model is optimized with applying rotor offset for the improvement of torque quality such as cogging torque and torque ripple. Furthermore, the electromagnetic power losses are analyzed, and their performance is comparatively evaluated. For the verification of analysis results, the IPMSM is manufactured, and its performance evaluation is also presented based on power loss and efficiency maps.**

***Index Terms*—efficiency, motor, loss, performance, synchronous.**

I. Introduction

A motor is a key technology for various industrial systems, such as electrical vehicles [1-2], machine tools [3], crane systems [4] and etc. As it is very well known, the machines are divided into asynchronous motors and synchronous motors according to the rotational speed difference between their rotor and rotating magnetic field. While an induction motor is a representative asynchronous motor, which is typical and most widely used in industrial area, the signs of diminishing interests in a wound rotor synchronous motor (WRSM) and an interior permanent magnet synchronous motors (IPMSM) have been not found yet, and their relative studies are being very actively performed.

The representative benefits of the WRSM are its low price due to no use of rare-earth magnets and wide control options due to the variable field current. Besides, it is very attractive that the machine is free from the irreversible demagnetization of PMs in spite of its relatively larger size owing to the brushes and slip rings. However, the maintenance cost of brushes and the vibration are still hot issues for motor designers. Therefore, in [5], the authors proposed blushless machine with third harmonic injection topology, and the study in [6] proposed asymmetrical rotor structure for torque ripple reduction. Those of previous works showed satisfied results in machine performance.

On the other hand, as shown in [7], IPMSMs have benefits of higher power density and efficiency than the other machine types. However, high cost of rare-earth PMs is still obstacle to be overcome.

Since both machine types have merits and demerits, they are required to be specifically compared. Therefore, in this paper, WRSM and IPMSM with 4 pole and 24 slot combination are comparatively investigated to provide readers reasonable opportunity for motor selection. The pole and slot combination is very popular as previously studied in [8]. Besides, the optimization of the rotors for each machine is performed by design of experiment (DOE) combined with response surface method (RSM) [9-10], while the design variables are rotor offset, tooth width and shoe thickness for the WRSM, and rotor offset, PM width and PM thickness for the IPMSM which have significant influence on motor voltage and torque characteristics. To demonstrate the validity of the electromagnetic field analysis performed in this paper, the analyzed results are compared with the measured values of a manufactured machine.

II. Optimized Design of WRSM and IPMSM Based on Surface Respond Method

Fig. 1 shows the analysis models of the WRSM and the IPMSM dealt with in this paper. Those machines have identical stator structure while the outer diameter and the stack length of the rotor core are also identical. In the stator, three-phase coil is placed, and 35PN250 from POSCO is employed for each core. In addition, for the WRSM, copper coil is also wound in the rotor core while Sm_2Co_{17} PMs with rectangle-shape are inserted into axial direction. More specific design specifications are presented in Table I, and the required torque and power characteristics are presented in Fig. 2.

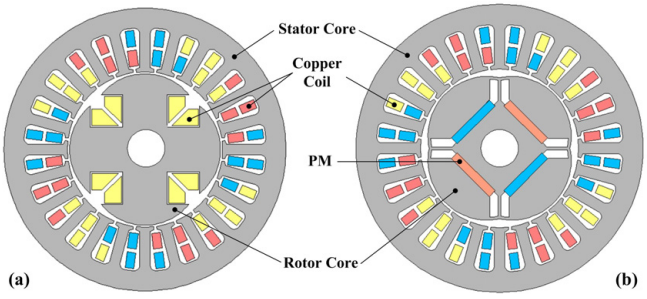

Figure 1. Analysis models with identical stator structure: (a) WRSM, (b) IPMSM

This was supported by Korea National University of Transportation in 2022.

Digital Object Identifier 10.4316/AECE.2022.02005

TABLE I. DESIGN SPECIFICATION OF ANALYSIS MODELS

Item	Unit	WRSM	IPMSM
Number of Poles	-	4	4
Number of Stator Slots	-	24	24
Rated Output Power	kW	1.2	1.2
Rated Speed	rpm	2,000	2,000
Rated Torque	Nm	5.7	5.7
Rated Current	Arms	17	17
Maximum Speed	rpm	10,000	10,000
Outer Diameter of Stator	mm	200	200
Inner Diameter of Stator	mm	110	110
Outer Diameter of Rotor	mm	108	108
Inner Diameter of Rotor	mm	26	26
Stack Length	mm	26	26
Number of Coil Turns per Phase	-	144	144
Number of Coil Turns per Slot	-	36	36
Number of Parallel Branch	-	1	1
Coil Pitch	-	5	5
Winding Connection	-	Y	Y
Predicted Phase Resistance	ohm	0.24	0.24
Measured Phase Resistance	ohm	-	0.26

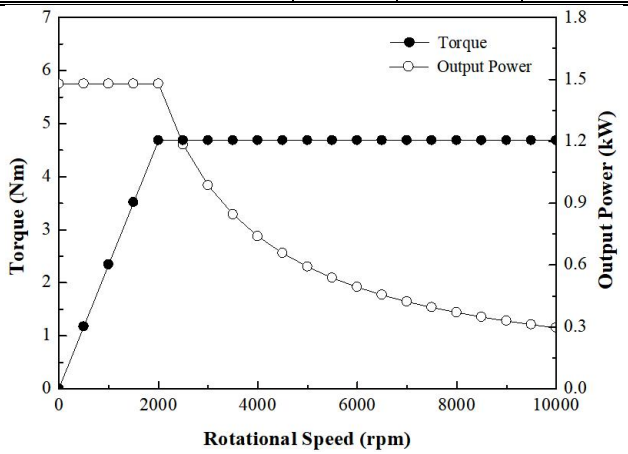

Figure 2. Required torque and output power characteristics according to rotational speed

As it is very well known, the voltage and torque of IPMSM can be derived by (1) and (2) [11]. As the author in the previous study mentioned, the voltage is determined by inverter type, so the possibility of operating speed can be predicted based on (1). In this paper, space vector pulse width modulation (SVPWM) inverter is employed, so the maximum value of phase voltage is approximately 53% of DC link voltage.

$$V_{ph}^2 = (R_a I_d - \omega L_q I_q)^2 + \left[R_a i_q + \omega(L_d i_d + \psi_a)\right]^2 \quad (1)$$

$$T = P[\psi_a i_q + (L_d - L_q) i_d i_q] \quad (2)$$

Since q-axis inductance of IPMSM is larger than its d-axis inductance, the negative d-axis current is required to achieve reluctance torque. On the other hand, when it comes to the WRSM, the d-axis inductance is larger than the q-axis, so positive d-axis current is required.

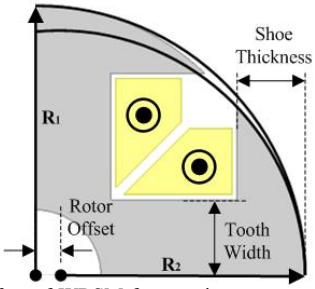

Figure 3. Rotor offset of WRSM for cogging torque reduction (1/4 partial model, R_1 - radius of offset in 0 mm, R_2 - radius of offset over 0 mm)

In this paper, to reduce cogging torque and to achieve better torque ripple characteristics, the rotor core of WRSM is optimally designed based on RSM. As design variables, rotor offset, tooth width and shoe thickness are determined due to their high influence on the motor performance as presented in Fig. 3. Here, R1 is the radius of the rotor with 0 mm of the offset, and R2 is the radius of the rotor with over 0 mm of the offset.

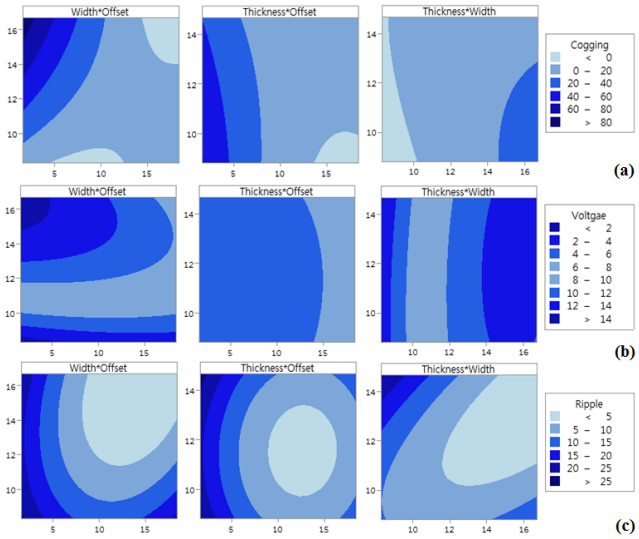

Figure 4. Contour maps of WRSM according to objective functions for optimization: (a) cogging torque, (b) phase voltage in no-load, (c) torque ripple

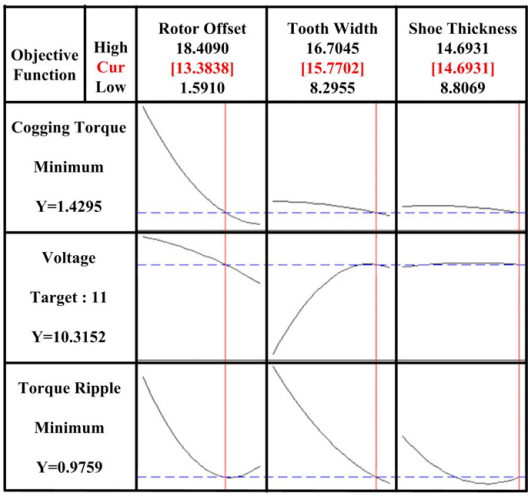

Figure 5. Rotor Optimization of WRSM based on response surface method (rotor offset: 13.4 mm, tooth width: 15.8 mm, shoe thickness: 14.7 mm)

While the constraint is the phase voltage 11 V in no-load condition, cogging torque and torque ripple are investigated as shown in Fig. 4, and the optimization results are presented in Fig. 5. By considering the manufacturing process, the rotor offset, tooth width and shoe thickness are determined as 13.4 mm, 15.8 mm and 14.7 mm for final model.

For the comparison with WRSM, the previously reported shape of IPMSM in [12] is newly optimized by the RSM with rotor offset as shown in Fig. 6 for this study. In the previous study, their analysis model was also 4 pole and 24 slot combination with inserted rectangular PMs.

The design variables for the rotor optimization are determined as rotor offset, PM width and PM thickness since they have high influence on motor performance as well. Besides, the objective functions are cogging torque

and torque ripple while the aimed induced voltage in no-load condition is 11 V.

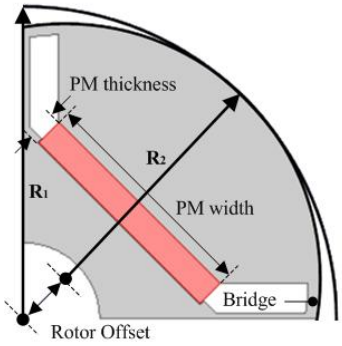

Figure 6. Rotor structure of IPMSM for comparative analysis with WRSM

In addition, for the reasonable comparison, the identical stator structure including copper coil layout is employed as that of WRSM.

On the other hand, NdFeB and Sm_2Co_{17} are known as the representative rare-earth PMs. Although the remanence of Sm_2Co_{17} is generally lower than that of NdFeB, its wide range of operating temperature is very attractive for various applications. In [13], the authors tested Sm_2Co_{17} at -196℃ by showing 6.5% higher remanence in comparison with room temperature condition. This paper also employed Sm_2Co_{17}, and the BH-curve of the magnet according to operating temperature is shown in Fig. 7.

In Fig. 8, contour maps of cogging torque, phase voltage and torque ripple according to the variation of the objective functions are presented. Based on the results, the rotor optimization results of the IPMSM are presented in Fig. 9, and the rotor offset, PM width and PM thickness are finally determined as 12.2 mm, 37.3 mm and 5.7 mm by considering the manufacturing process.

The THD and torque ripple can be improved by adopting appropriate winding layout. In [14], the authors performed comparative analysis of IPMSMs with 10 poles and 12 slots combination based on finite element method, and it suggested various multi-layer winding types by considering torque characteristics, power loss and efficiency.

Besides, as shown in [15], the double layer is widely employed due to the superior quality of loss and torque ripple characteristics while the single layer can increase the fundamental winding factor. In the study, it was shown that the double layer can completely cancel the sub-harmonics which have high influence on loss, noise and vibration.

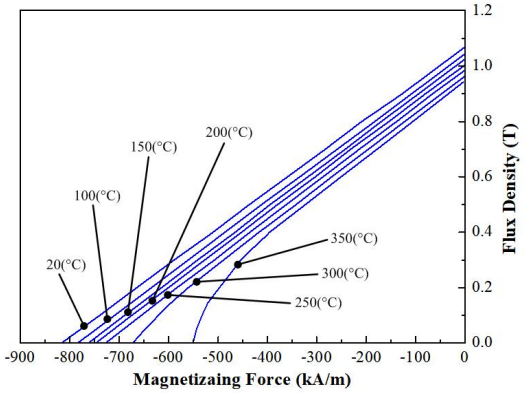

Figure 7. B-H curve of Sm_2Co_{17} according to operating temperature

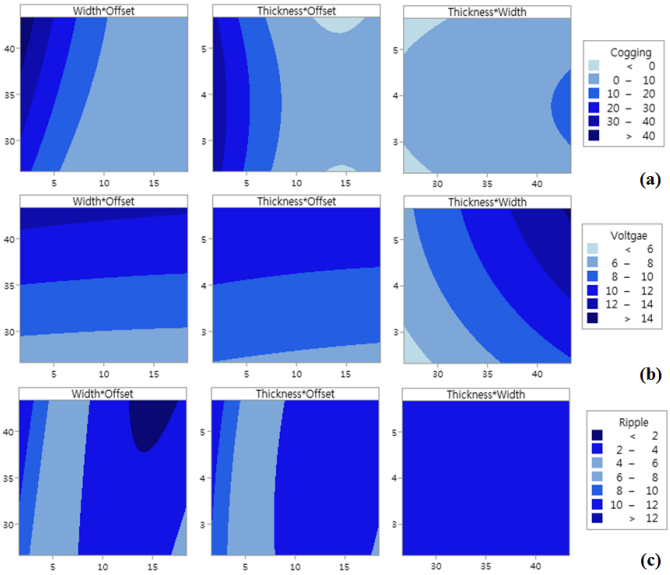

Figure 8. Contour maps of IPMSM according to objective functions for optimization: (a) cogging torque, (b) phase voltage in no-load, (c) torque ripple

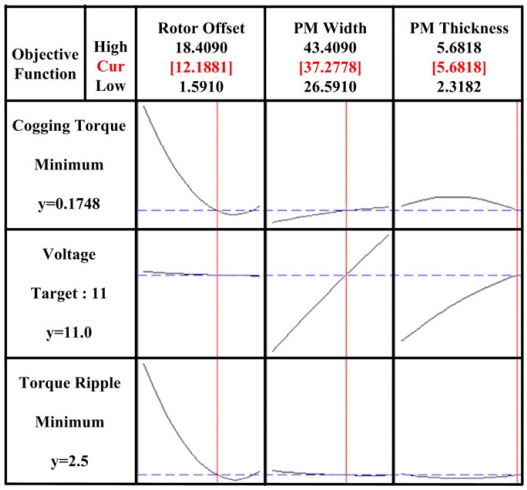

Figure 9. Rotor optimization of IPMSM based on response surface method (rotor offset: 12.2 mm, PM width: 37.3 mm, PM thickness: 5.7 mm)

The performance of the WRSM and the IPMSM dealt with in this paper can be also improved by the stator coil winding layouts, and Fig. 10 presents the considered arrangements. On the other hand, in some applications, the flat conductors such as hairpin can be employed to improve fill factor and power density, but its manufacturing cost is very high [16]. Therefore, this study applied widely used round coil, and its fill factor is approximately 40%.

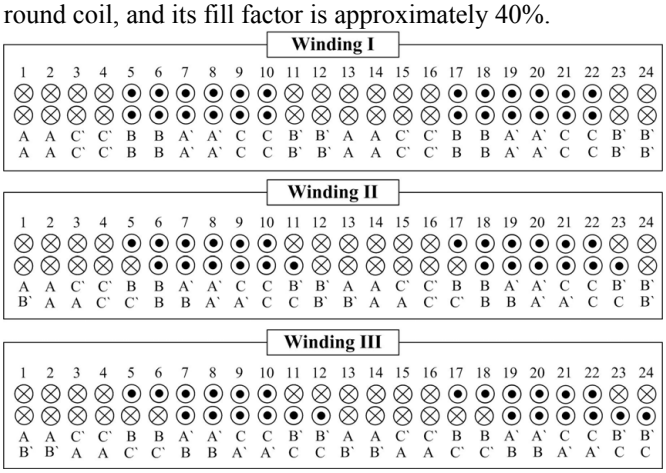

Figure 10. Stator coil winding layout for both WRSM and IPMSM: (a) winding I, (b) winding II, (c) winding III

As presented before, based on the RSM, the optimum values of the rotor cores are found while the induced voltage of each machine is determined to be identical for fair comparison. Not only is the *rms* value important, but also its THD value is also critical for motor performance in that they are directly related to the torque ripple.

According to winding layouts presented above, the induced voltage waveforms are compared in Fig. 11, and their FFT results are presented in Fig. 12 and Table II. As can be confirmed in those figures and table, Winding III shows lowest THD, but its reduction of entire induced voltage value is relatively higher than the others, so Winding II is determined to be applied.

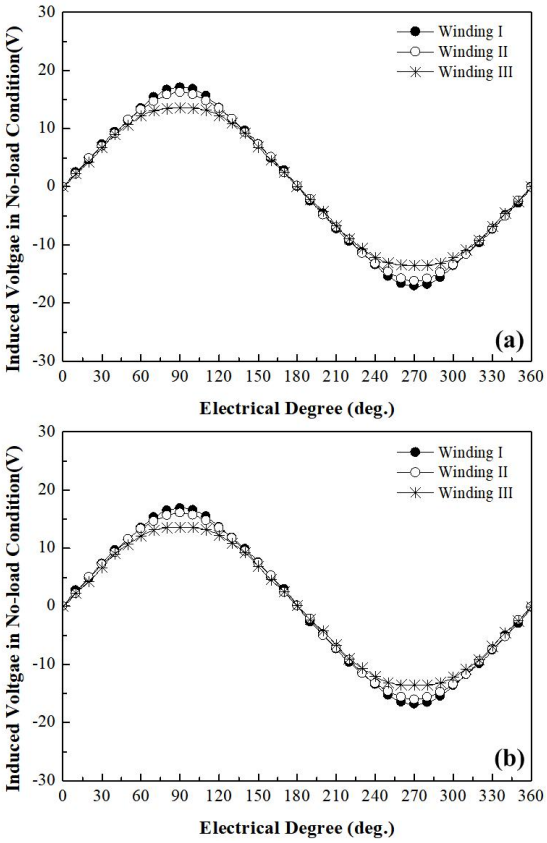

Figure 11. Induced voltage in no-load condition according to stator coil winding layouts: (a) WRSM, (b) IPMSM

In Fig. 13, by applying Winding II, the analyzed induced voltage of the WRSM and the IPMSM are compared with the finally optimized rotors presented above. It can be confirmed that they are very well corresponded to each other.

When it comes to resistance, 20°C of operating temperature is considered, and it is calculated by multiplying the resistivity by the length of the coil by the inversed value of the cross-sectional area of the coil. The predicted and measured resistance values are presented in Table I.

On the other hand, as previously reported in [17], d-axis and q-axis inductance values are varied according to current and load angle. In this study, the d-axis and the q-axis inductance values are derived by (3)-(6) [18]. Here, Ψ_0, Ψ_a, and α are respectively flux linkage in no-load condition, flux linkage in load-condition and angle difference of those flux linkage waveforms. For each WRSM and IPMSM, positive and negative values are employed for I_a.

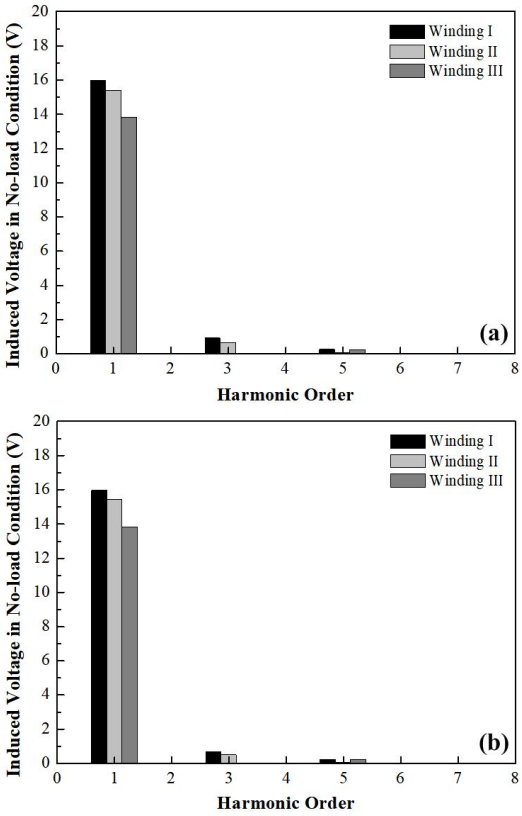

Figure 12. FFT results of induced voltage in no-load condition according to stator coil winding layouts: (a) WRSM, (b) IPMSM

TABLE II. THD OF WRSM AND IPMSM ACCORDING TO COIL WINDING

Item	Unit	WRSM	IPMSM
Winding I	%	6.07	4.67
Winding II	%	4.38	3.42
Winding III	%	1.95	1.85

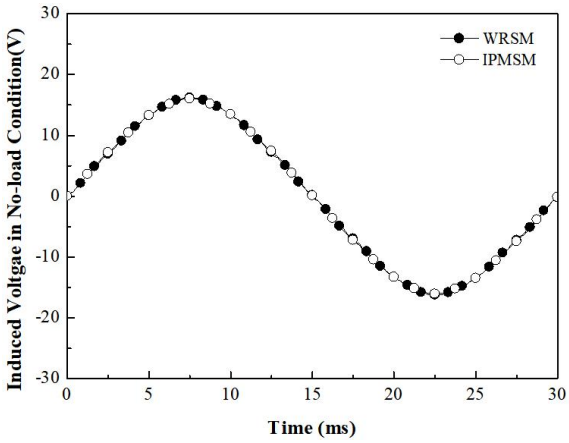

Figure 13. Induced phase voltage of finally designed WRSM and IPMSM in no-load condition at 1000 rpm

Based on the equations for the inductance derivation, the achieved values are presented in Fig. 14 according to machine types.

$$L_d = (\psi_0 \cos\alpha - \psi_a)/i_d \quad (3)$$

$$L_q = (\psi_0 \sin\alpha)/i_q \quad (4)$$

$$i_d = I_a \sin\beta \quad (5)$$

$$i_q = I_a \cos\beta \quad (6)$$

The torque of the WRSM and the IPMSM dealt with in this paper can be largely divided into cogging torque, magnetic torque and reluctance torque.

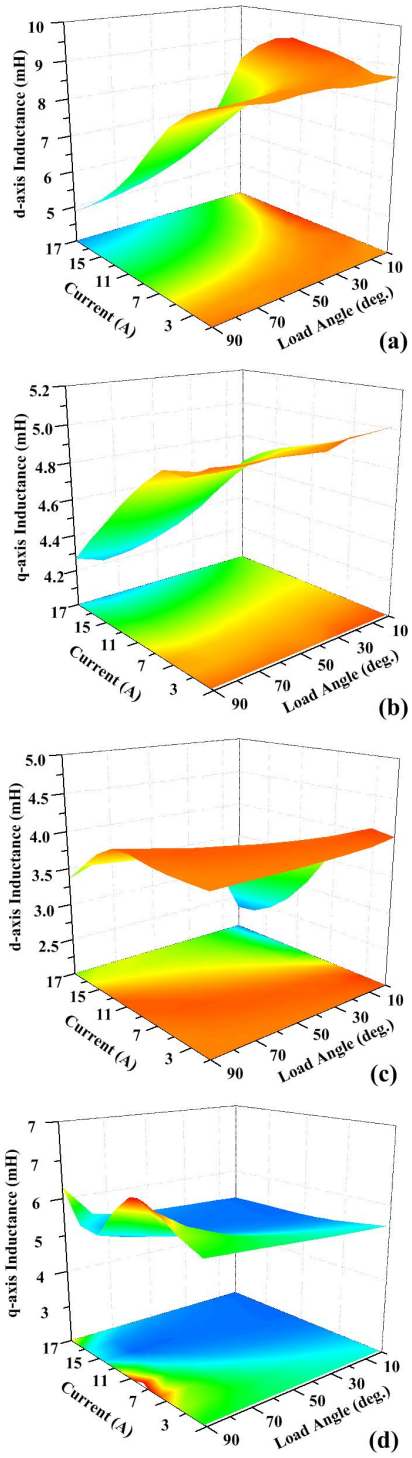

Figure 14. Inductance variation according to current and load angle: (a) L_d of WRSM, (b) L_q of WRSM, (c) L_d of IPMSM, (d) L_q of IPMSM

Cogging torque is the unbalanced force due to the magnetic structure of rotor and stator cores without the consideration of armature current.

On the other hand, the magnetic torque and reluctance torque are generated with armature current while it results in fluctuations called as torque ripple. As it is very well known, the reduction of cogging torque and torque ripple is essential in motor design stage for lower vibration and noise levels.

Above all, the cogging torque in no-load condition can be explained by (7) [19]. Here, α and θ are rotor position angle and circumferential direction while $Br(\theta)$, h_m and g are respectively radial component of flux density of PM, length of magnetization direction and air-gap length.

$$W = \frac{1}{2\mu_0}\int_V B_r^2(\theta)\left(\frac{h_m(\theta)}{h_m(\theta)+g(\theta,\alpha)}\right)^2 dv \qquad (7)$$

In Fig. 15, the analyzed cogging torque characteristics are compared according to machine types. As shown in the figure, IPMSM shows lower peak-to-peak value of the cogging torque, and *24nth* harmonic orders are confirmed [20]. Here, *n* is positive integer.

On the other hand, as mentioned before, the torque of the WRSM and the IPMSM in load condition can be identically expressed by (1). Differently from IPMSM whose load angle is in second quadrant, L_d of WRSM is larger than L_q, so the load angle is located in first quadrant [21].

In Fig. 16, the torque characteristics of both machines according to load angle are compared. As shown in the figure, the maximum torque of the WRSM is higher than the IPMSM, but as the load angle becomes higher, the torque of the IPMSM shows higher values.

In Fig. 17 a), their torque ripple values are also compared in load condition at 17(A) with the load angle of maximum torque. It can be known that 2.8% of the IPMSM is higher than 1.9% of the WRSM. In Fig. 17 b), FFT results are presented, and the 6^{th} and 12^{th} harmonic orders show visible values. While the fundamental order of the IPMSM shows less value, 6^{th} and 12^{th} harmonic orders show difference between those machines.

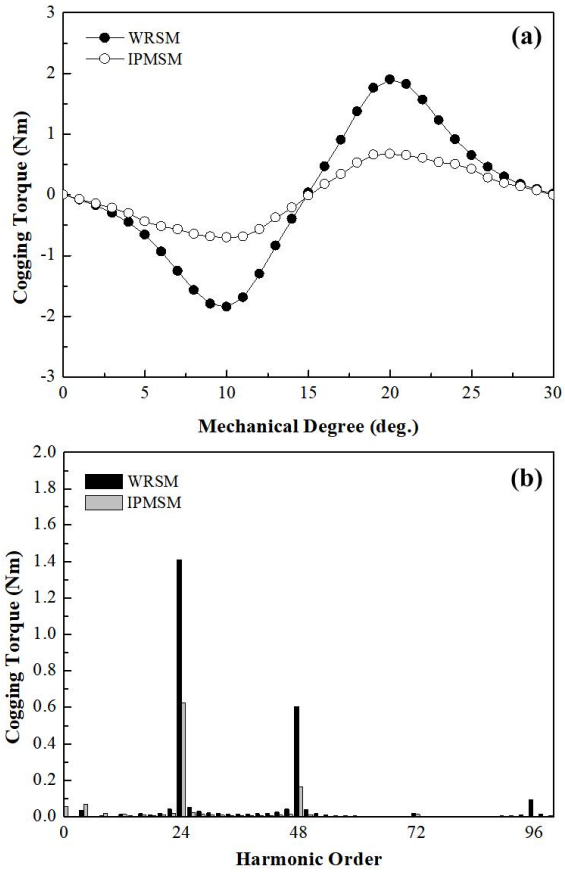

Figure 15. Cogging torque characteristic according to machine type in no-load condition: (a) waveform of 1/12 mechanical cycle, (b) FFT results

When it comes to IPMSM, since the thicker bridge of the rotor indicated in Fig. 6 causes higher flux leakage, its thickness should be minimized while it satisfies the mechanical strength. In [22], the authors proposed separated pole piece which is very good idea, but the analysis models in this paper are too small to employ the structure.

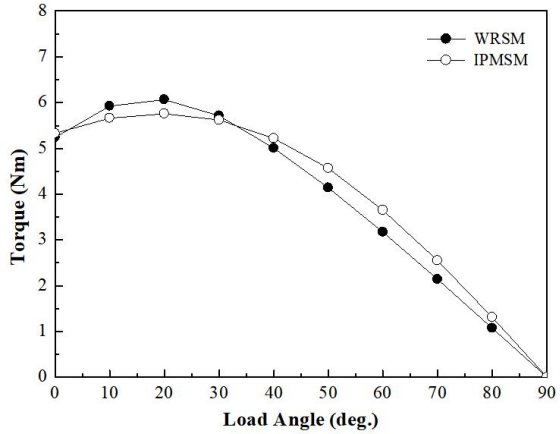

Figure 16. Torque versus load angle according machine types (17A)

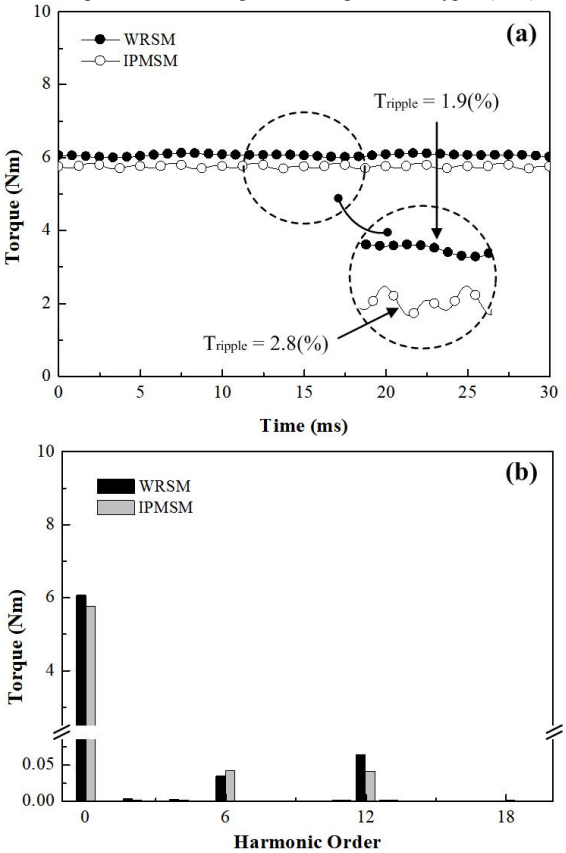

Figure 17. Torque ripple characteristics according to machine types: (a) waveform (1000 rpm), (b) FFT results

On the other hand, the stress analysis of the IPMSM is performed to confirm the safety probability of the rotor bridge. The mechanical properties of the rotor core are presented in Table III [23], and *Von Mises Equivalent Stress* is applied which were analytically derived in [24]. Consequently, the centrifugal force derived by (8) and *Von Mises Equivalent Stress* by (9) are presented in Fig. 18 [24]. Here, M , ω and r are mass, angular speed and radius while σ_r, σ_θ and σ_z are radial stress, circumferential stress and axial load, respectively.

$$F_c = M\omega^2 r \tag{8}$$

$$\sigma_{VM} = \sqrt{\frac{1}{2}\left\{(\sigma_r-\sigma_\theta)^2+(\sigma_\theta-\sigma_z)^2+(\sigma_z-\sigma_r)^2\right\}} \tag{9}$$

As shown in the Table III, the yield point of rotor core 35PN250 is 370 N/mm^2, and the analysis results of *Von Mises Equivalent Stress* show the value at approximately 14000 rpm. Since the maximum speed of the analysis model is 10000 rpm, the bridge is determined to be safe during its operation.

TABLE III. MECHANICAL PROPERTIES OF ROTOR CORE 35PN250

Item	Unit	Value
Density	Kg/m^3	7600
Elastic Modulus	GPa	200
Poisson ratio	-	0.3
Yield Strength	MPa	370

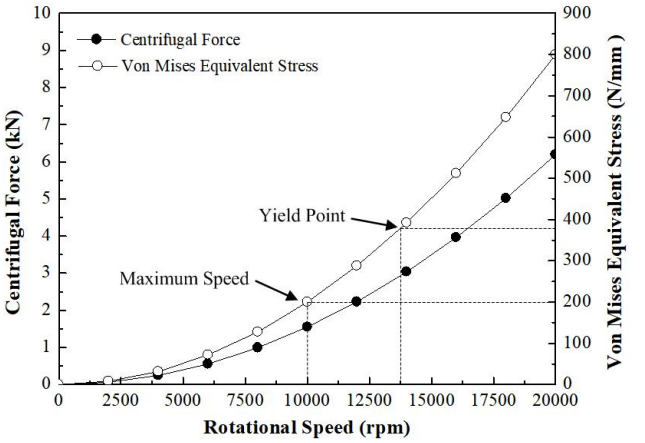

Figure 18. Analyzed centrifugal force and Von Mises Equivalent Stress according to rotational speed

Although the 2D FEM has generally high reliability, this paper manufactured one of the analysis machines for experimental verification. In Fig. 19 a), the rotor and stator cores which were made by wire-cutting method are presented, and Fig. 19 b) is the laminated stator assembly with three phase winding coils. Based on the constructed experimental set in Fig. 19 c), the motor performance evaluation was performed.

At first, in no-load condition, the induced phase voltage are measured at 1000 rpm as presented in Fig. 20, and it shows very well corresponded values in comparison with the analyzed results.

On the other hand, although the machines dealt with in this paper should be operated by an inverter with the field weakening control, it is not addressed in this study.

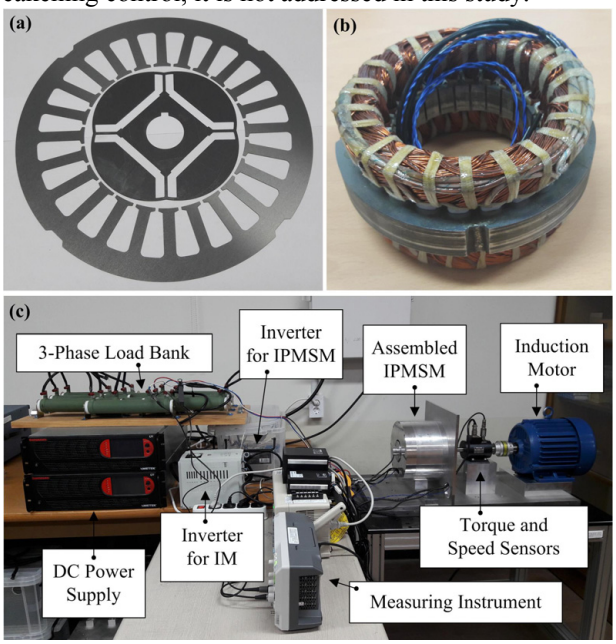

Figure 19. Manufactured IPMSM: (a) rotor and stator cores, (b) stator winding assembly, (c) experimental set construction

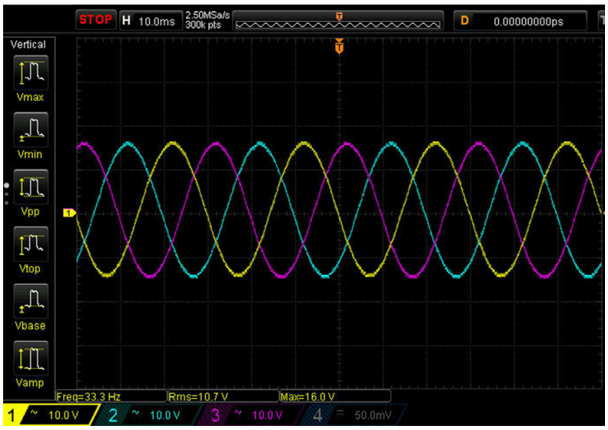

Figure 20. Induced phase voltage of manufactured IPMSM in no-load condition at 1000 rpm

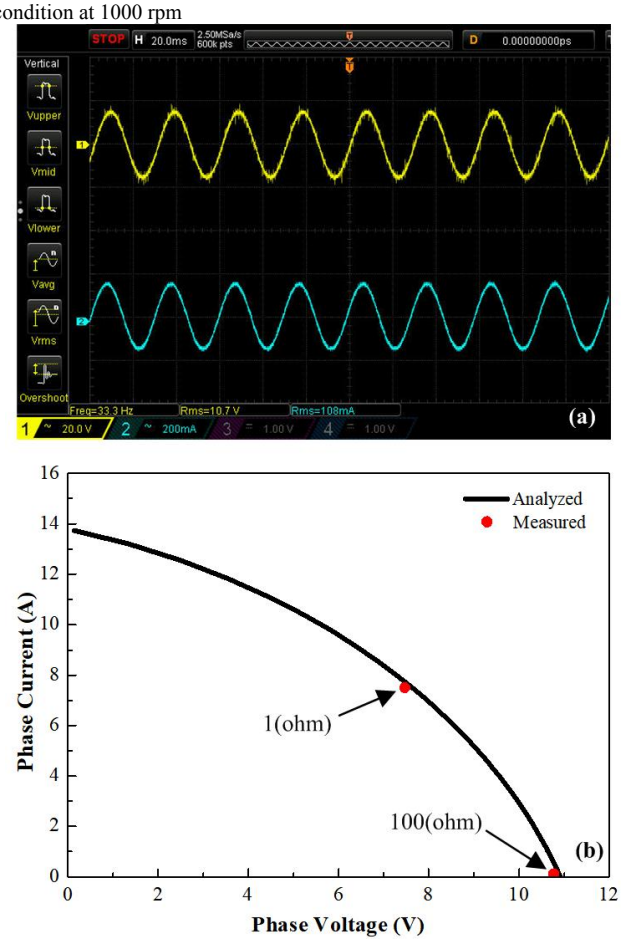

Figure 21. Voltage and current characteristic comparison in generating mode at 1000 rpm: (a) voltage and current waveform, (b) voltage and current curve according to load variation

However, as an alternative, the generating mode is additionally analyzed and measured to demonstrate the validity of the analysis results. Since the validity of the induced voltage is confirmed before, the load voltage comparison between analysis and experiment can also validate other equivalent circuit parameters, such as resistance and inductance.

First of all, in Fig. 21, the voltage and current power curve are measured when the machine is operated in generator mode. In this experiment, the induction machine makes mechanical input power while the value of load resistance is varied to achieve the voltage and current characteristic in Fig. 21. As can be confirmed in the figure, the measured values are very well corresponded to the analyzed results.

The copper loss due to stator coil winding can be determined by (10) while the WRSM has additional loss in rotor winding which can be calculated by (11). Here, R_{stator} and R_{rotor} are respectively the resistance of stator coil winding and the resistance of rotor coil winding.

$$P_{copper\_Stator} = 3 \cdot I^2 \cdot R_{stator} \tag{10}$$

$$P_{copper\_Rotor} = I^2 \cdot R_{rotor} \tag{11}$$

On the other hand, the core loss and rotor loss can be estimated by (12) [25]. Here, h, e and a are hysteresis loss, eddy current loss, and excess loss while k is the coefficient of each loss.

$$P_{core} = k_h f B + k_e f^2 B^2 + k_a f^{1.5} B^{1.5} \tag{12}$$

From Fig. 22 and Fig. 23, the efficiency can be compared while the motor is controlled according to aimed torque and speed conditions. Since the WRSM has additional copper loss in rotor side, its value is generally higher than the IPMSM. Furthermore, in high speed conditions, the field weakening capability of the IPMSM is much superior to that of the WRSM, its core loss is much lower than WRSM. Finally, efficiency map is presented as shown in the figures, and it can be confirmed that the high efficiency can be achieved between 3000 rpm and 4000 rpm.

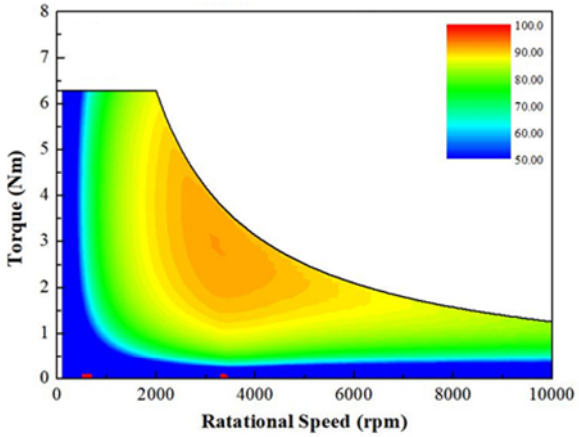

Figure 22. Efficiency map of WRSM according to rotational speed

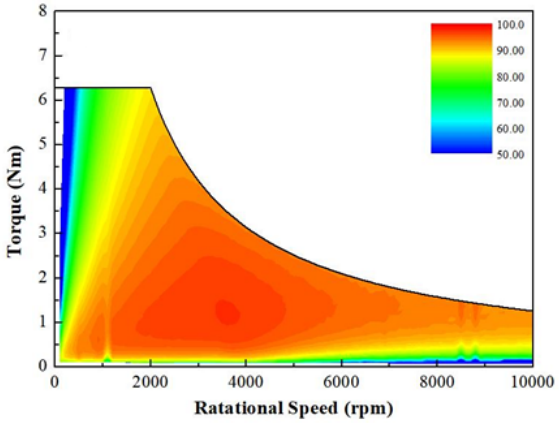

Figure 23. Efficiency map of IPMSM according to rotational speed

III. CONCLUSION

From the comparative investigation, following conclusion can be made under the identical size conditions. When it comes to torque performance, WRSM shows superior values in both average torque and torque ripple. Therefore, for the less noise and vibration, it can be attractive candidate. However, WRSM shows high cogging torque values, and it requires extra space for brush and slip rings. On the other

hand, IPMSM shows much higher efficiency in wide operating speed due to the less power loss. Since it does not have copper winding, copper loss in rotor side does not exist. Therefore, in this size and output power conditions, IPMSM is better choice for machine design.

REFERENCES

[1] J. H. Choi, Y. D. Chun, P. W. Han, M. J. Kim, D. H. Koo, J. Lee, J. S. Chun, "Design of high power permanent magnet motor with segment rectangular copper wire and closed slot opening on electrical vehicles," IEEE Transactions on Magnetics, vol. 46, no. 6, 2070-2073, Jun. 2010. doi:10.1109/TMAG.2010.2041908

[2] P. Palacky, P. Brandstetter, P. Chlebis, V. Sladecek, P. Simonik, D. Slivka, "Control algorithms of propulsion unit with induction motors for electric vehicle," Advances in Electrical and Computer Engineering, vol. 14, no. 2, pp. 69-76, Apr. 2014. doi:10.4316/AECE.2014.02012

[3] M. Sridharbabu, T. Kosaka, N. Matsui, "Design reconsiderations of high speed permanent magnet hybrid excitation motor for main spindle drive in machine tools based on experimental results of prototype machine", IEEE Transactions on Magnetics, vol. 47, no. 10, pp. 4469-4472, Oct. 2011. doi:10.1109/TMAG.2011.2156400

[4] N. Mitrovic, V. Kostic, M. Petronijevic, B. Jeftenic, "Multi-motor drives for crane application," Advances in Electrical and Computer Engineering, vol. 9, no. 3, pp. 57-62, Oct 2009. doi:10.4316/AECE.2009.03011

[5] G. Jawad, Q. Ali, T. A. Lipo, B. I. Kwon, "Novel brushless wound rotor synchronous machine with zero-sequence third-harmonic field excitation," IEEE Transactions on Magnetics, vol. 52, no. 7, pp. 8106104, Jul. 2016. doi:10.1109/TMAG.2015.2512281

[6] S. I. Park, K. C. Kim, "Torque ripple reduction method with asymmetric pole for wound-field synchronous motor," IEEE Transactions on Magnetics, vol. 51, no. 3, pp. 8102504, Mar. 2015. doi:10.1109/TMAG.2014.2357853

[7] T. A. Huynh, M. F Hsieh, "Comparative study of PM assisted SynRM and IPMSM on constant power speed range for EV applications," IEEE Transactions on Magnetics, vol. 53, no. 11, pp. 8211006, Nov. 2017. doi:10.1109/TMAG.2017.2707125

[8] D. K. Woo, B. H. Jeong, "Irreversible demagnetization of permanent magnet in a surface-mounted permanent magnet motor with overhang structure," IEEE Transactions on Magnetics, vol. 52, no. 4, pp. 8102606, Apr. 2016. doi:10.1109/TMAG.2015.2476782

[9] L. Fang, J. W. Jung, J. P. Hong, J. H. Lee, "Study on high-efficiency performance in interior permanent-magnet synchronous motor with double-layer PM design," IEEE Transactions on Magnetics, vol. 44, no. 11, pp. 4393-4396, Nov. 2008. doi:10.1109/TMAG.2008.2002001

[10] J. Y. Lee, J. H. Chang, D. H. Kang, S. I. Kim, J. P. Hong, "Tooth shape optimization for cogging torque reduction of transverse flux rotary motor using design of experiment and response surface methodology," IEEE Transactions on Magnetics, vol. 43, no. 4, pp. 1817-1820, Apr. 2007. doi:10.1109/TMAG.2007.892611

[11] S. G. Lee, "A study on the improvement of output torque and cogging torque reduction of interior permanent magnet synchronous motor for direct drive of washing machine," The Transactions of KIEE, vol. 68P, no. 1, pp.6-10, 2019. doi:10.5370/KIEEP.2019.68.1.006

[12] I. Tanaka, H. Nitomi, L. Imanishi, K. Okamura, H. Yashiki, "Application of high-strength nonoriented electrical steel to interior permanent magnet synchronous motor," IEEE Transactions on Magnetics, vol. 48, no. 6, pp. 2997-3001, Jun. 2013. doi:10.1109/TMAG.2012.2236101

[13] C. Guo, S. Huang, J. Wang, Y. Feng, Q. Wang, "Design of cryogenic permanent magnet synchronous motor for submerged liquefied natural gas pump," IEEE Transactions on Magnetics, vol. 54, no. 11, pp. 8207405, Nov. 2018. doi:10.1109/TMAG.2018.2832005

[14] A. S. Abdel-Khalik, S Ahmed, A. M. Massoud, "Effect of multilayer windings with different stator winding connections on interior PM machines for EV applications," IEEE Transactions on Magnetics, vol. 52, no. 2, pp. 8100807, Feb. 2016, doi:10.1109/TMAG.2015.2495301

[15] G. Dajaku, W. Xie, D. Gerling, "Reduction of low space harmonics for the fractional slot concentrated windings using a novel stator design," IEEE Transactions on Magnetics, vol. 50, no. 5, pp. 8201012, May 2014. doi:10.1109/TMAG.2013.2294754

[16] Y. J. Oh, H. C. Liu, S. Y. Cho, J. H. Won, H. W. Lee, J. Lee, "Design, modeling and analysis of a railway traction motor with independently rotating wheelsets," IEEE Transactions on Magnetics, vol. 54, no. 11, pp. 8205305, Nov. 2018. doi:10.1109/TMAG.2018.2842433

[17] X. Zhu, S. Yang, Y. Du, Z. Xiang, L. Xu, "Electromagnetic performance analysis and verification of a new flux-intensifying permanent magnet brushless motor with two-layer segmented permanent magnets," IEEE Transactions on Magnetics, vol. 52, no. 7, pp. 8204004, Jul. 2016. doi:10.1109/TMAG.2016.2519465

[18] Y. K. Kim, "A study of design for interior permanent magnet synchronous motor by using d-q axis equivalent circuit method", Journal of the Korean Magnetics Society, vol. 27, no. 2, 54-62, Apr. 2017. doi:10.4283/JKMS.2017.27.2.054

[19] J. H. Lee, Y. S. Park, "Characteristic analysis of interior permanent synchronous machine by considering magnetization patterns," Journal of Magnetics, vol. 23, no 2, pp. 267-273, Jun. 2018. doi:10.4283/JMAG.2018.23.2.267

[20] H. S. Ko, K. J. Kim, "Characterization of noise and vibration sources in interior permanent magnet brushless DC motors," IEEE Transactions on Magnetics, vol. 40, no. 6, pp. 3482-3489, Nov. 2004. doi:10.1109/TMAG.2004.832991

[21] H. S. Seol, J. M. Jeong, J. Lee, C. S. Jin, "Current control of WRSM considering magnetic saturation phenomenon," IEEE Transactions on Magnetics, vol. 52, no. 7, pp. 8204104, Jul. 2016. doi:10.1109/TMAG.2016.2526075

[22] W. H. Kim, I. S. Jang, C. S. Jin, J. Lee, S. G. Lee, "Design of novel overhang structure for separated pole-piece type ferrite magnet motor," IEEE Transactions on Magnetics, vol. 51, no. 3, pp. 8202004, Mar. 2015. doi:10.1109/TMAG.2014.2346081

[23] Y. D. Chun, B. G. Park, D. J. Kim, J. H. Choi, P. W. Han, S. K. Lee, "Development and performance investigation on a 60kW induction motor for EV propulsion," Journal of Electrical Engineering Technology, vol 11, no. 3, pp. 639-643, May 2016. doi:10.5370/JEET.2016.11.3.639

[24] S. M. Barrans, M. M. J. Al-Ani, and J. Carter, "Mechanical design of rotors for permanent magnet high speed electric motors for turbocharger applications," IET Electrical Systems in Transportation, vol. 7, no. 4, pp. 278-286, Dec. 2017. doi:10.1049/iet-est.2016.0081

[25] K. Yamazaki, N. Fukushima, "Iron-loss modeling for rotating machines: Comparison between Bertotii's three-term expression and 3-D eddy-current analysis," IEEE Transactions on Magnetics, vol. 46, no. 8, pp. 3121-3124, Aug. 2010, doi:10.1109/TMAG.2010.2044384